Journal of Catalysis 283 (2011) 149–160

Contents lists available at SciVerse ScienceDirect

Journal of Catalysis

journal homepage: www.elsevier.com/locate/jcat

Identification of the chemical state of Fe in barium hexaaluminate using Rietveld refinement and ^{57}Fe Mössbauer spectroscopy

Yanyan Zhu [a,b], Xiaodong Wang [a,*], Aiqin Wang [a], Guotao Wu [a], Junhu Wang [a], Tao Zhang [a,*]

[a] State Key Laboratory of Catalysis, Dalian Institute of Chemical Physics, Chinese Academy of Sciences, Dalian 116023, People's Republic of China
[b] Graduate University of Chinese Academy of Sciences, Beijing 100049, People's Republic of China

ARTICLE INFO

Article history:
Received 4 May 2011
Revised 14 July 2011
Accepted 1 August 2011
Available online 13 September 2011

Keywords:
Hexaaluminate
Chemical state of Fe
Rietveld refinement
Mössbauer spectroscopy
N_2O decomposition

ABSTRACT

The catalytic activity of hexaaluminate is closely related to the chemical state of substituted active metal ions. In this paper, the mechanism of stabilization of Fe ions in β_l-Al_2O_3 and magnetoplumbite-type Fe-substituted Ba hexaaluminates was proposed at the molecule level on the basis of X-ray diffraction, Rietveld refinement, and Mössbauer spectroscopy. Fe^{3+} ions originated from oxidic entities dispersed on Ba-modified γ-Al_2O_3 mainly entered into the sites in the loosely packed mirror plane of the hexaaluminates. In particular, Fe^{3+} ions at low concentration preferentially occupied the tetrahedral Al(5) sites of the β_l-Al_2O_3 phase, while Fe^{3+} ions at high concentration mainly occupied the trigonal bipyramidal Al(5) and octahedral Al(3) sites in the magnetoplumbite phase. Meanwhile, tetrahedral Fe^{3+} ions in the intermediate spinel-type $BaAl_2O_4$ phase preferentially entered into the tetrahedral Al(2) sites in the spinel block of hexaaluminates. Fe ions in the Al(5) sites of β_l-Al_2O_3 and the Al(3) sites of magnetoplumbite phase were highly active for N_2O decomposition.

1. Introduction

Metal-substituted hexaaluminates are attractive catalysts for high-temperature applications, e.g., catalytic combustion of methane [1–5], CO_2 reforming of methane [6], partial oxidation of methane [7–9], process-gas N_2O abatement [10–12], and the decomposition of N_2O as a propellant [13–16]. These materials exhibit stable phase composition up to 1600 °C and remarkable resistance to sintering and thermal shock [1,2]. These unique and excellent properties are associated with their peculiar layered structure, consisting of alternate stacking along the *c* axis of closely packed spinel blocks and loosely packed mirror planes in which large cations are located. The chemical formula of metal-substituted hexaaluminates can be represented by $AM_xAl_{11-x}O_{17-\alpha}$ or $AM_xAl_{12-x}O_{19-\alpha}$, corresponding to β-Al_2O_3 or magnetoplumbite (MP) structures with the same space group, $P6_3/mmc$ (No. 194), where A stands for a large alkaline, alkaline earth, or rare earth cation, and M represents a 3*d* transition metal ion (e.g., Mn, Fe, Ni, Co, Cu) in an Al crystallographic site, which acts as an active center for a variety of catalytic reactions.

Among transition metals, Mn and Fe have been reported as the most effective promoters for CH_4 catalytic combustion [17,18] and N_2O decomposition [11,12,15]. So far, most reports have concentrated on Mn-substituted hexaaluminates, in which the oxide state and crystallographic sites of Mn were found to be closely related to the catalytic activity. Groppi et al. [19] and Artizzu-Duart et al. [20] observed enhanced CH_4 combustion activity with the increase of the Mn^{3+}/Mn^{2+} ratio. Our previous work [15] also revealed that octahedral Mn^{3+} in Al(1) sites was much more active for N_2O decomposition than tetrahedral Mn^{2+} in Al(2) sites. Moreover, Li and Wang [21] and Astier et al. [22] claimed that Mn^{3+} ions located in the Al interstitial sites near the mirror plane were highly reactive toward Mn^{3+}/Mn^{2+} redox cycles and CH_4 catalytic combustion, compared with those in deep positions in the rigid spinel block. As for the states of Fe in hexaaluminates, there are some arguments. Groppi et al. [23] suggested that tetrahedral Fe^{3+} and small numbers of Fe^{2+} ions were present in Ba hexaferrite. However, Lietti et al. [18] and Artizzu-Duart et al. [20] reported that Fe ions in Ba hexaaluminate were in a trivalent state in octahedral coordination. Naoufal et al. [24] further revealed that framework Fe^{3+} ions were located in four different octahedral sites (S1–S4) and tentatively attributed the methane combustion activity to Fe^{3+} in S1 and S2 sites.

In contrast to Mn, which only substituted for a very limited number of Al ions, and excess Mn existing as catalytically inactive Mn oxides outside the hexaaluminate framework, Fe could completely replace Al and lead to the formation of a $BaFe_{12}O_{19}$ hexaferrite structure. The experimental finding elucidated that the mechanism of stabilization of Mn and Fe ions in the hexaaluminate structure was very different. Groppi et al. [25] proposed a forma-

* Corresponding authors. Fax: +86 411 84691570.
E-mail addresses: xdwang@dicp.ac.cn (X. Wang), taozhang@dicp.ac.cn (T. Zhang).

0021-9517/$ - see front matter © 2011 Elsevier Inc. All rights reserved.
doi:10.1016/j.jcat.2011.08.001

tion route for unsubstituted barium hexaaluminate, namely solid-state reactions between γ-Al_2O_3 and dispersed barium compounds, or $BaAl_2O_4$. With regard to the metal-substituted hexaaluminate, Groppi et al. [19,26] and Yalfani et al. [27] found that the presence of Mn and Fe in the precursors could promote the diffusion of large cations (Ba^{2+} and La^{3+}) in a γ-Al_2O_3 matrix and then lead to the formation of hexaaluminates at lower calcination temperatures by means of X-ray diffraction. However, there was still not a clear picture of how the transition metal ions were stabilized in the hexaaluminate structure, which is very important for understanding the final metal chemical state in the target hexaaluminate phase and thus the effects on the catalytic properties. This may be due to the complex high-temperature solid-state reaction for the formation of hexaaluminate, which is very difficult to characterize.

Fe, which can be studied by sensitive ^{57}Fe Mössbauer spectroscopy, may act as a pioneer for the investigation of the local environments of substituted transition metal ions in hexaaluminate. In this paper, we explored the evolution of Fe from amorphous precursor to Fe-substituted barium hexaaluminate and proposed a mechanism of stabilization of Fe ions in hexaaluminate at the molecular level. In particular, Rietveld refinement and Mössbauer spectroscopy were employed to identify the Fe valence and crystallographic sites in the hexaaluminate structure, which were discussed in connection with catalytic activity in high-concentration N_2O decomposition.

2. Experimental

2.1. Catalyst preparation

$BaFe_xAl_{12-x}O_{19-\alpha}$ samples with $x = 0$–4 (denoted as BF*x*A-*t*; when $x = 0$, BF*x*A-*t* = BA-*t*; *t* indicates calcination temperature) were prepared using the carbonate route as reported [15,28]. For example, to prepare BF1A-*t*, $Ba(NO_3)_2$, $Fe(NO_3)_3{\cdot}9H_2O$, and $Al(NO_3)_3{\cdot}9H_2O$ with the molar ratio 1:1:11 were dissolved individually in deionized water at 60 °C, and then added into a saturated aqueous solution of $(NH_4)_2CO_3$ under strong stirring to form the hexaaluminate precursor precipitate. After continuous stirring at 60 °C for 6 h, the precipitate was filtered, washed with deionized water, and then dried at 120 °C overnight. To understand the evolution of chemical states of Fe, the sample was calcined in air at 500, 700, 900, 1000, 1100, and 1200 °C for 4 h to obtain BF1A-500, BF1A-700, BF1A-900, BF1A-1000, BF1A-1100, and BF1A-1200, respectively. For comparison, F1A-*t* and F3A-*t*, similarly to BF1A-*t* and BF3A-*t* samples, were prepared by the above coprecipitation procedure but without $Ba(NO_3)_2$ in the starting materials.

2.2. Catalyst characterization

The X-ray diffraction (XRD) patterns were recorded with a PANalytical X'Pert-Pro powder X-ray diffractometer, using Cu Kα monochromatized radiation ($\lambda = 0.1541$ nm). A PDF database was used for phase analysis. Crystalline dimensions were determined from the Debye–Scherrer equation. Phase composition and the positions of Fe ions were adjusted by Rietveld full-profile analysis using WinPLOTR (April 2008 version). The metal content of samples was determined by X-ray fluorescence (XRF). BET surface areas of the catalysts were measured by N_2 adsorption at −196 °C using a Micromeritics ASAP 2010 apparatus. Scanning electron microscopy (SEM) experiments were performed with a JSM 6360-LV electron microscope operating at 20–25 kV. The samples were vapor-deposited with gold before analysis. The Mössbauer spectra were recorded at room temperature with a spectrometer working in the mode of constant acceleration with a ^{57}Co γ-quantum source in Rh matrix. The absorbers were obtained by pressing the powdered samples (about 10 mg/cm^2 of natural iron). Samples after H_2 reduction were protected under Ar during Mössbauer measurements. All spectra were computer-fitted to a Lorentzian shape with a least-squares fitting procedure. The isomer shifts (IS) were given with respect to the centroid of α-Fe at room temperature.

2.3. Activity test

Catalytic performance was evaluated in a fixed-bed quartz tube reactor using 100 mg (20–40 mesh) of a catalyst diluted with quartz sand as described previously [13–15]. Prior to the reaction, the catalyst sample was prereduced with pure H_2 at 400 °C for 2 h. After cooling to room temperature in Ar, the gas flow was switched to the reacting gas mixture containing 30 vol.% N_2O in Ar at a flow rate of 50 ml/min, corresponding to a gas hourly space velocity of 30,000 h^{-1}. The outlet gas composition was analyzed online with an Agilent 6890 N gas chromatograph equipped with Porapak Q and Molecular Sieve 13X columns and a thermal conductivity detector. N_2O conversion was calculated from the difference between the inlet and outlet concentrations. Before analysis, the reaction proceeded for 30 min at each temperature to reach a steady state.

3. Results

3.1. Phase composition

Fig. 1 shows the XRD patterns of BF1A-*t* and BF3A-*t* samples obtained by calcination of precursors at different temperatures. For comparison, F1A-*t* and F3A-*t* samples were also characterized by XRD.

For BF1A (Fig. 1a), calcination of precursors at 500 °C resulted in amorphous structure except for a trace of microcrystalline $BaCO_3$ [JCPDS 1-506]. After calcination at 700 °C, broad modulations of the baseline were detected and attributed to γ-Al_2O_3 [JCPDS 1-1308]. In addition, the most intense (202) reflection ($2\theta = 28.3°$) of $BaAl_2O_4$ [JCPDS 1-72-387] could also be verified, indicating that a small amount of Ba compounds and γ-Al_2O_3 was transformed into $BaAl_2O_4$. No iron oxide species was detected by XRD in either BF1A-500 or BF1A-700, probably due to the very small crystalline size, below the determined limit (3 nm). Taking into account the molar ratio of Ba:Fe:Al = 1:1:11 and high BET surface areas (188–301 m^2/g) of both samples, Fe species should be highly dispersed on the Ba-modified γ-Al_2O_3. Further calcination at 900 and 1000 °C resulted in the appearance of remarkable $BaAl_2O_4$ peaks accompanied by unexhausted γ-Al_2O_3. The cell parameter a_0 ($a_0 = b_0$) of $BaAl_2O_4$ in BF1A-900 (10.441 Å) was larger than that in the Fe-free BA-900 sample ($a_0 = 10.435$ Å), indicating that larger Fe ions (0.64 Å) entered into the structure of $BaAl_2O_4$ by replacing smaller Al^{3+} (0.51 Å). Calcination at 1000 °C led to the shift of spectra to slightly lower 2θ values corresponding to the expansion of the cell parameter ($a_0 = 10.453$ Å) of $BaAl_2O_4$, implying that more Fe ions entered into $BaAl_2O_4$. When the calcination temperature was raised to $T \geqslant 1100$ °C, it is noteworthy that the formation of a β-Al_2O_3 hexaaluminate phase took place, together with the consumption of γ-Al_2O_3 and $BaAl_2O_4$. The cell parameters a_0 ($a_0 = b_0$) and c_0 of the hexaaluminate phase in BF1A-1100 and BF1A-1200 were 5.610–5.614 and 22.768–22.775 Å, respectively, both of which were significantly larger than in the unsubstituted BA-1200 sample ($a_0 = 5.589$ Å, $c_0 = 22.744$ Å), implying the presence of Fe ions in the hexaaluminate lattice. From the above results, we deduced that Fe ions in the hexaaluminate structure should originate from these Fe species in the precursors, which were dis-

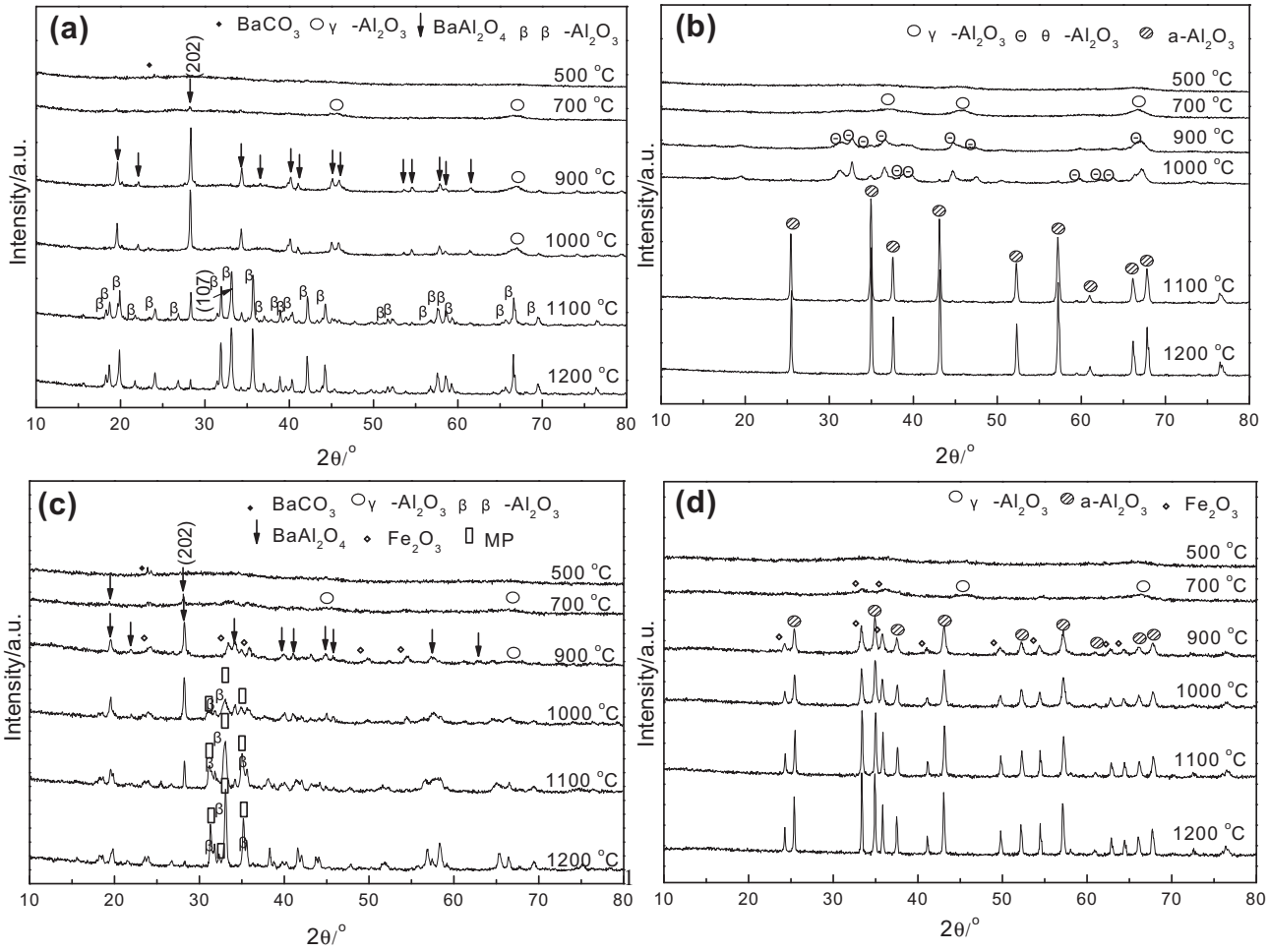

Fig. 1. X-ray diffraction patterns of: (a) BF1A-*t*, (b) F1A-*t*, (c) BF3A-*t*, and (d) F3A-*t* samples.

persed on the Ba-modified γ-Al_2O_3 and located in the intermediate $BaAl_2O_4$ phase.

In the case of F1A (Fig. 1b), samples calcined at 500 and 700 °C consisted of microcrystalline γ-Al_2O_3. When the calcination temperature was increased further, γ-Al_2O_3 was transformed into θ-Al_2O_3 and α-Al_2O_3. In particular, after calcination at 1100 and 1200 °C, F1A presented rather sharp diffraction peaks of α-Al_2O_3 due to extensive sintering of particles. The absence of iron oxide species in F1A-*t* indicated that Fe species were highly dispersed on γ-Al_2O_3 or dissolved in alumina, evidenced by the enlarged cell parameters of θ-Al_2O_3 and α-Al_2O_3.

For BF3A (Fig. 1c), with a larger amount of Fe ions, the absence of Fe_2O_3 diffraction peaks was still observed after calcination at 500 and 700 °C, indicating that the crystalline size of Fe_2O_3 was still below the determined limit (3 nm) at a lower calcination temperature. As compared to BF1A-700, $BaAl_2O_4$ peaks in BF3A-700 became stronger, indicating that the increase of Fe content promoted the formation of $BaAl_2O_4$. Thus, one would expect more Fe ions to enter into the $BaAl_2O_4$ structure after 900 °C calcination, which was evidenced by the enlargement of the cell parameter a_0 of $BaAl_2O_4$ (10.467 Å for BF3A-900 vs. 10.441 Å for BF1A-900). Besides γ-Al_2O_3 and $BaAl_2O_4$, the remarkable peaks of Fe_2O_3 were also present, and the crystalline size estimated from the broadening of the diffraction peaks was 18 nm, which might result from the increase of Fe content and the large drop of BET surface areas from 700 to 900 °C (167 m^2/g vs. 81 m^2/g). The increase of Fe content promoted the formation of the hexaaluminate phase that occurred at 1000 °C, below the threshold temperature of 1100 °C observed in BF1A, which was attributed to the promoting effect of Fe on the mobility of Ba^{2+} in the γ-Al_2O_3 matrix [23,27]. On further calcination at 1100 and 1200 °C, besides the diffraction peaks of β-Al_2O_3 hexaaluminate, peaks at $2\theta = 31.3°$ and 35.1° were also clearly observed, which were associated with the MP-type hexaaluminate [6,19,23]. Obviously, Fe content influences the crystal structure of Ba hexaaluminates.

For F3A (Fig. 1d), 500 °C calcination resulted in amorphous structure without any Fe_2O_3 diffraction peaks. After calcination at 700 °C, Fe_2O_3 peaks were already present, whereas no iron oxide species was detected in Ba-containing BF3A-700, indicating that the dispersion of Fe oxides was greatly promoted by the presence of Ba^{2+}. When the calcination temperature was above 900 °C, besides the direct formation of α-Al_2O_3 resulting from γ-Al_2O_3, the diffraction peaks of Fe_2O_3 became sharper due to severer sintering of particles; e.g., the crystalline size significantly increased from 25 nm at 900 °C to 46 nm at 1200 °C. This was quite different from Ba-containing BF3A, where the crystalline size of Fe_2O_3 was only 18 nm at 900 °C and the intensities of Fe_2O_3 diffraction peaks decreased greatly with increasing calcination temperature, and eventually disappeared upon calcination at 1200 °C. The examination of Fe content by XRF revealed no Fe loss after 1200 °C calcination in

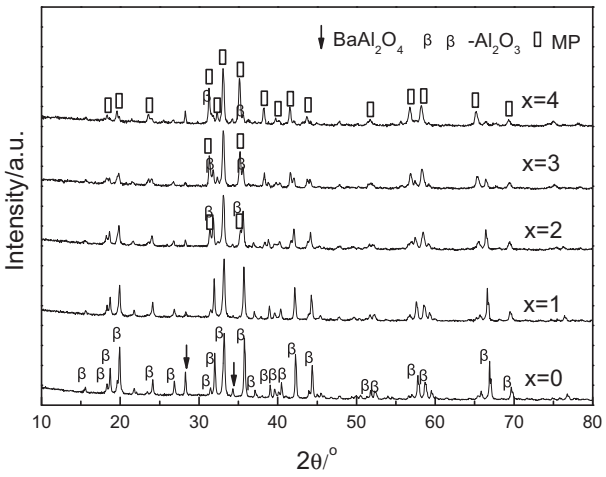

Fig. 2. X-ray diffraction patterns of BF*x*A-1200 (x = 0–4) samples.

either F3A or BF3A. The above results suggested that the hexaaluminate structure offered a better dispersion of Fe species under high-temperature conditions than the α-Al_2O_3 structure.

Fig. 2 illustrates the XRD patterns of BF*x*A-1200 (x = 0–4). When x = 0 and 1, well-crystallized β-Al_2O_3 hexaaluminate phase was observed. However, when x = 2, reflections at 2θ = 31.3° and 35.1° corresponding to MP-type hexaaluminate were also detected, implying that more Fe content promoted the formation of MP phase. When x increased to 3, the diffraction peaks due to the MP phase became stronger, while those corresponding to the β-Al_2O_3 phase became weaker. In particular, when x = 4, the β-Al_2O_3 peaks had almost disappeared. The result strongly suggested that the increase of introduced Fe ions in the hexaaluminate structure resulted in the phase transformation from β-Al_2O_3 into MP. This was consistent with the previous report that the β-Al_2O_3 phase formed in the region of Al-rich composition and the MP phase formed in the region of Fe-rich composition [23]. It is worthwhile to note that no iron oxide was detected even in BF4A-1200, which is different from what happened in other transition-metal-substituted Ba hexaaluminates (such as Mn and Cu) [4,15,20,29,30], in which excess metal ions usually lead to the appearance of metal oxides outside the hexaaluminate framework.

3.2. Rietveld refinement

To quantify the amounts of both β-Al_2O_3 and MP phases, Rietveld analysis of the XRD powder data was performed for BF*x*A-1200 (x = 1–4) and the corresponding results are listed in Table 1. The increase of Fe content significantly influenced the proportions of different phases, but not the compositions of the β-Al_2O_3 and MP phases. The MP phase presented a higher Fe concentration than the β-Al_2O_3 phase; for example, the compositions of the MP and β-Al_2O_3 phases in BF3A-1200 were $BaFe_{4.39}Al_{7.61}O_{19}$ and $Ba_{0.78}Fe_{0.79}Al_{10.21}O_{17.28}$, respectively. Compared with the cell parameter ($a_0 = b_0$ = 5.614–5.616 Å) of the β-Al_2O_3 phase in BF*x*A-1200 (x = 1–4), the MP phase with x = 2–4 had a higher a_0 value (5.710–5.715 Å), confirming that more Fe ions entered into the Al crystallographic sites in the MP structure. However, somewhat surprising is that the c_0 value of the MP phase (22.644–22.650 Å) was smaller than that of β-Al_2O_3 (22.775–22.781 Å), although the former had a larger amount of Fe ions. This was caused by the increased Ba concentration of the MP phase, which enforced the bonds between the spinel block and the mirror plane and resulted in the contraction of the mirror plane. This contraction compensated for the expansion along the c axis due to the incorporation of Fe ions with a higher concentration. Such a compensation effect was also observed in Mn-substituted Ba hexaaluminate [29], where the larger size of Mn^{2+} ions (0.80 Å) was balanced by the contraction of the mirror plane. It is noteworthy that the phase transformation from β-Al_2O_3 to MP resulted in the stabilization of Fe-substituted Ba hexaaluminate through a charge compensation mechanism, which was quite different from the Mn-substituted Ba hexaaluminate with only a β-Al_2O_3 phase. In the Mn-substituted Ba^{2+}-β-Al_2O_3, the excess Ba^{2+} charge (with respect to +1.5, which was regarded as the ideal valence for the large cation in the mirror plane of the stoichiometric β-Al_2O_3 phase according to the electrostatic valence rule [31]) was compensated for by the substitution of Mn^{2+} ions with a lower charge than Al^{3+} ions, which decreased the Reidinger defect and resulted in the stabilization of Mn-substituted Ba^{2+}-β-Al_2O_3. In contrast, in the Fe-substituted Ba hexaaluminate, the excess cation charge in Ba^{2+}-β-Al_2O_3 was compensated for by the formation of a charge-insufficient Ba^{2+}-MP phase, where +2.4 was assumed as the ideal valence at the large cation sites [31].

Subsequently, the crystallographic sites of Fe in both β-Al_2O_3 and MP phases were carefully analyzed. Fig. 3 shows the typical fitted XRD patterns of BF1A-1200 with a β-Al_2O_3 structure and BF3A-1200 with both β-Al_2O_3 and MP phases, and the corresponding results are summarized in Table 2.

It is reported [32] that unsubstituted Ba-β-Al_2O_3 hexaaluminate is constituted by a defective Ba-poor β_I phase and a Ba-rich β_{II} phase, with compositions $Ba_{0.72}Al_{11}O_{17.28}$ and $Ba_{1.16}Al_{10.68}O_{17.16}$, respectively. Comparing our obtained XRD data of BF1A-1200 with the diffraction patterns of β_I-Al_2O_3 and β_{II}-Al_2O_3 phases, the Ba-β_I-Al_2O_3 structure [31,32] was chosen as the starting model for Rietveld refinement. The analysis results confirmed that a Ba-poor β_I-Al_2O_3 phase with $Ba_{0.79}Fe_{0.79}Al_{10.21}O_{17.29}$ indeed formed in BF1A-1200, in line with Mn-substituted Ba-β_I-Al_2O_3 hexaaluminates [29]. In β_I-Al_2O_3 structure (Fig. 4a), small fractions of Al^{3+}

Table 1
Rietveld refinement results of BF*x*A-1200 (x = 1–4).

Results	x = 1	x = 2	x = 3	x = 4
Rp	12.115	12.484	10.274	11.771
Rwp	15.619	16.461	13.882	15.465
Phase composition (molar ratio)	98% β_I-Al_2O_3[a], 2% $BaAl_2O_4$	80% β_I-Al_2O_3, 18% MP, 2% $BaAl_2O_4$	46% β_I-Al_2O_3, 53% MP, 1% $BaAl_2O_4$	6% β_I-Al_2O_3, 89% MP, 5% $BaAl_2O_4$
Composition of β_I-Al_2O_3 phase	$Ba_{0.79}Fe_{0.79}Al_{10.21}O_{17.29}$	$Ba_{0.78}Fe_{0.79}Al_{10.21}O_{17.28}$	$Ba_{0.78}Fe_{0.79}Al_{10.21}O_{17.28}$	$Ba_{0.78}Fe_{0.79}Al_{10.21}O_{17.28}$
$a_0 = b_0$ (Å)	5.614	5.614	5.615	5.616
c_0 (Å)	22.775	22.776	22.778	22.781
Composition of MP phase	–	$BaFe_{4.37}Al_{7.63}O_{19}$	$BaFe_{4.39}Al_{7.61}O_{19}$	$BaFe_{4.45}Al_{7.55}O_{19}$
$a_0 = b_0$ (Å)	–	5.710	5.712	5.715
c_0 (Å)	–	22.644	22.647	22.650

[a] One type of β-Al_2O_3 hexaaluminate.

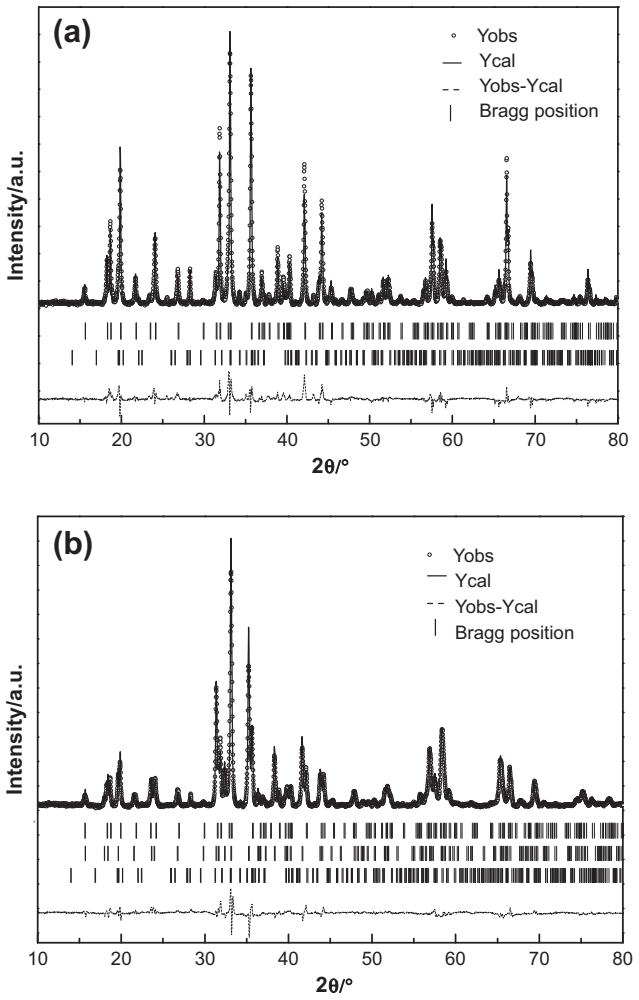

Fig. 3. X-ray diffraction patterns fitted using the Rietveld refinement method for: (a) BF1A-1200 and (b) BF3A-1200 samples.

ions shifted from their normal octahedral Al(1) sites in the spinel block to new tetrahedral interstitial Al(5) sites in the mirror plane bridged by interstitial oxygen, due to the vacancy of Ba^{2+} through a Reidinger defect mechanism [31]. Refinements of the Al occupancies for BF1A-1200 indicated the presence of Fe ions in the tetrahedral Al(2) sites in the spinel block and the tetrahedral interstitial Al(5) sites in the mirror plane of β_l-Al_2O_3, while Al(1), Al(3), and Al(4) sites did not show any significant evidence of Fe substitution (Table 2). This was quite different from the case of Mn-substituted Ba-β_l-Al_2O_3, where only the sites Al(1) and Al(2) in the spinel block were substituted for by Mn [29]. Such a difference in the mirror plane may be responsible for the phase transformation of Fe-substituted barium hexaaluminates from β_l-Al_2O_3 into MP, since the structure type of hexaaluminates was determined by the composition and the defectivity of the mirror plane [23,33].

In the 46% β_l-Al_2O_3 phase of BF3A-1200, Fe ions only occupied Al(2) and interstitial Al(5) sites, as in BF1A-1200 (Table 2). In the 53% MP phase, the refinement results revealed that all of the Al crystallographic sites (Al(1), Al(2), Al(3), Al(4), and Al(5)) could be occupied by Fe ions. In particular, the occupancies of Fe in Al(2), Al(3), and Al(5) sites were above 60%, indicating that Fe ions had preference to occupy the tetrahedral Al(2) sites in the spinel block, and octahedral Al(3) and trigonal bipyramid Al(5) sites in the mirror plane (Fig. 4b). The Fe site occupancy of β_l-Al_2O_3 and MP in BF2A-1200 and BF4A-1200 samples was close to that in BF3A-1200; accordingly no detailed data are shown.

3.3. ^{57}Fe Mössbauer spectroscopy

Fig. 5 shows room-temperature fitted Mössbauer spectra of BF1A-*t*, F1A-*t*, BF3A-*t*, and F3A-*t*, and the corresponding Mössbauer parameters are listed in Table 3. It can be seen that the isomer shift (IS) values (0.20–0.41 mm/s) are much more related to those of Fe^{3+} species (IS = 0.17–0.42 mm/s) [34–36] rather than to those of Fe^{2+} species (for which usual values of IS are closer to 0.9–1.3 mm/s [37–39]). This result indicates that iron ions in our samples are exclusively in the +3 oxidation state.

For BF1A (Fig. 5a) calcined at 500 and 700 °C, the observed doublet was assigned to small superparamagnetic Fe_2O_3 species highly dispersed on the Ba-modified γ-Al_2O_3, as the Fe^{3+} concentration was very low, just one-tenth of the Al^{3+} concentration (denoted as Fe^{3+} (low concentration)). Upon calcination at 900 and 1000 °C, besides the doublet corresponding to Fe^{3+} (low concentration), one new doublet with a relatively low QS value (0.66–0.71 mm/s) was also observed, indicating the formation of a new Fe-containing species. Taking into account the appearance of $BaAl_2O_4$ at these temperatures and the enlargement of the cell parameter of $BaAl_2O_4$, the new doublet was attributed to Fe^{3+} in hexagonal spinel-type $BaAl_2O_4$, since the hyperfine parameters (IS = 0.25–0.27 mm/s, QS = 0.66–0.71 mm/s, Table 3) were close to those of the subspectrum (IS = 0.28 mm/s, QS = 0.80 mm/s) corresponding to Fe^{3+} ions in the $BaAl_2O_4$ structure reported in a $(Ba_{0.5}Sr_{0.5})(Fe_{0.8}Al_{0.2})O_3$ sample [40]. Fig. 6 displays the crystal structure of $BaAl_2O_4$. One can see that every aluminum atom has four oxygen atoms as close neighbors. Therefore, Fe^{3+} ions incorporated into $BaAl_2O_4$ should be located in the tetrahedral (Th) sites, by replacing Al^{3+}. These results imply that there were two chemical states of Fe^{3+} before the formation of hexaaluminate, namely, Fe^{3+} ions in oxidic entities dispersed on Ba-modified γ-Al_2O_3 and Fe^{3+}(Th) in $BaAl_2O_4$. The relative area (*A*) in Table 3 shows that more Fe^{3+} ions that originated from oxidic entities entered into the $BaAl_2O_4$ lattice from 900 to 1000 °C (17 vs. 25%), which was in accordance with the increased trend of the cell parameter of $BaAl_2O_4$, probably because a higher calcination temperature can offer more energy for Fe^{3+} ions to dig into the rigid spinel $BaAl_2O_4$ structure. When the calcination temperature was further increased to 1100 and 1200 °C with the formation of the major phase of β_l-Al_2O_3 hexaaluminate, two new quadrupole doublets were assigned to different Fe^{3+} species in the β_l-Al_2O_3 structure, except for a small doublet corresponding to residual Fe^{3+}(Th) in $BaAl_2O_4$ of BF1A-1100. The IS values (0.20–0.23 mm/s) of the two new doublets were small and much more related to Fe^{3+} ions in Th sites (IS = 0.18–0.19 mm/s) reported in $CaFe_{1.2}Al_{10.8}O_{19}$ [34] and $LaFeAl_{11}O_{19}$ [41], indicating that Fe^{3+} ions occupied Th sites in β_l-Al_2O_3 structure, which was consistent with the Rietveld refinement result. One doublet with a small QS value (0.60 mm/s) was assigned to Fe^{3+}(Th) in symmetric Al(2) sites of the β_l-Al_2O_3 structure. The QS value (1.01–1.03 mm/s) of the other doublet was relatively high. It was assigned to Fe^{3+} ions in the distorted tetrahedral interstitial Al(5) sites resulting from the Reidinger defect, since the higher QS value means there was a greater extent of electric field distortion around Fe^{3+} ions [24,34]. The chemical state of Fe^{3+}(Th) in Al(2) in the spinel block of β_l-Al_2O_3 was similar to that of Fe^{3+}(Th) in the intermediate spinel-type $BaAl_2O_4$ phase, evidenced by the close QS values (0.60 mm/s vs. 0.66–0.71 mm/s); meanwhile, close QS values of Fe^{3+}(Th) in Al(5) in the mirror plane of β_l-Al_2O_3 (1.01–1.03 mm/s) and Fe^{3+} ions in oxidic entities (1.07–1.11 mm/s) were also observed. This suggested that Fe^{3+}(Th) in $BaAl_2O_4$ and Fe^{3+} ions that originated from oxidic entities in the precursors entered into the Al(2) and Al(5) sites in the final β_l-Al_2O_3 hexaaluminate materials, respectively.

In the case of F1A-*t* (Fig. 5b), Fe species initially existed as small superparamagnetic Fe_2O_3 species dispersed on γ-Al_2O_3. As the

Table 2
Refined sites occupancy of Ba, Fe, and Al in BF1A-1200 and BF3A-1200.

Atom site	Mult.[a]	Coor.[b]	Block	BF1A-1200	BF3A-1200	
				β_l-Al_2O_3	β_l-Al_2O_3	MP
Ba(1)	2	–	M[c]	0.787	0.784	1.00
Al(1)	12	Oh[d]	S[e]	0.929	0.928	0.808
Al(2)	4	Th[f]	S	0.799	0.799	0.386
Al(3)	4	Th/Oh[g]	M	1.00	1.00	0.320
Al(4)	2	Oh	S	1.00	1.00	0.960
Al(5)[h]	12	Th	M	0.006	0.007	–
Al(5)[i]	2	Tr[j]	M	–	–	0.391
Fe in Al(1)	12	Oh	S	–	–	0.192
Fe in Al(2)	4	Th	S	0.201	0.201	0.614
Fe in Al(3)	4	Th/Oh	M	–	–	0.680
Fe in Al(4)	2	Oh	S	–	–	0.040
Fe in Al(5)[h]	12	Th	M	0.065	0.065	–
Fe in Al(5)[i]	2	Tr	M	–	–	0.609
Ratio of Fe in different sites				51:49[k]	24:38:31:7[l]	

[a] Multeity.
[b] Coordination.
[c] Mirror plane.
[d] Octahedral.
[e] Spinel block.
[f] Tetrahedral.
[g] Tetrahedral for the β_l-Al_2O_3 phase or octahedral for MP phase.
[h] Interstitial Al(5) in the β_l-Al_2O_3 phase.
[i] Al(5) in MP phase.
[j] Trigonal bipyramid.
[k] The ratio of Fe in Al(2) and Al(5) sites in the β_l-Al_2O_3 phase.
[l] The ratio of Fe in Th-Al(5) of the β_l-Al_2O_3 phase, Th-Al(2) of both the β_l-Al_2O_3 and MP phases, and Oh and Tr sites in the MP phase.

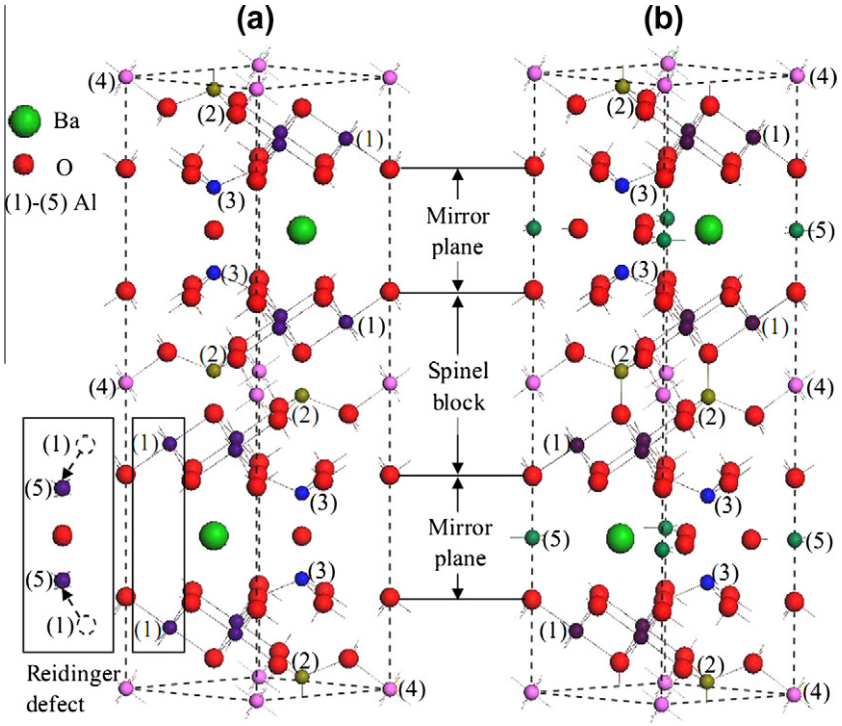

Fig. 4. The structure of Ba-hexaaluminate: (a) β_l-Al_2O_3 and (b) MP. Numbers in parentheses refer to the different Al sites. Al(1), octahedral site; Al(2), tetrahedral site; Al(3) in β_l-Al_2O_3, tetrahedral site; Al(3) in MP, octahedral site; Al(4), octahedral site; Al(5) in β_l-Al_2O_3, tetrahedral site; Al(5) in MP, trigonal bipyramid site.

calcination temperature increased, Fe^{3+} ions originated from oxidic entities entered into the alumina structure, accompanied by the phase transition γ-$Al_2O_3 \rightarrow \theta$-$Al_2O_3 \rightarrow \alpha$-$Al_2O_3$.

For BF3A (Fig. 5c) calcined at 500 and 700 °C, the doublet corresponding to small superparamagnetic Fe_2O_3 species dispersed on the Ba-modified γ-Al_2O_3 was also observed, although the Fe^{3+} concentration was as high as one-third of the Al^{3+} concentration (denoted as Fe^{3+} (high concentration)). After calcination at 900 °C, besides a doublet (26%) assigned to Fe^{3+}(Th) in $BaAl_2O_4$, a combination of the superparamagnetic doublet (39%) and the magnetic sextet (35%) appeared with the increased crystalline size of Fe_2O_3 (from below 3 nm at 700 °C to around 18 nm at 900 °C). This indi-

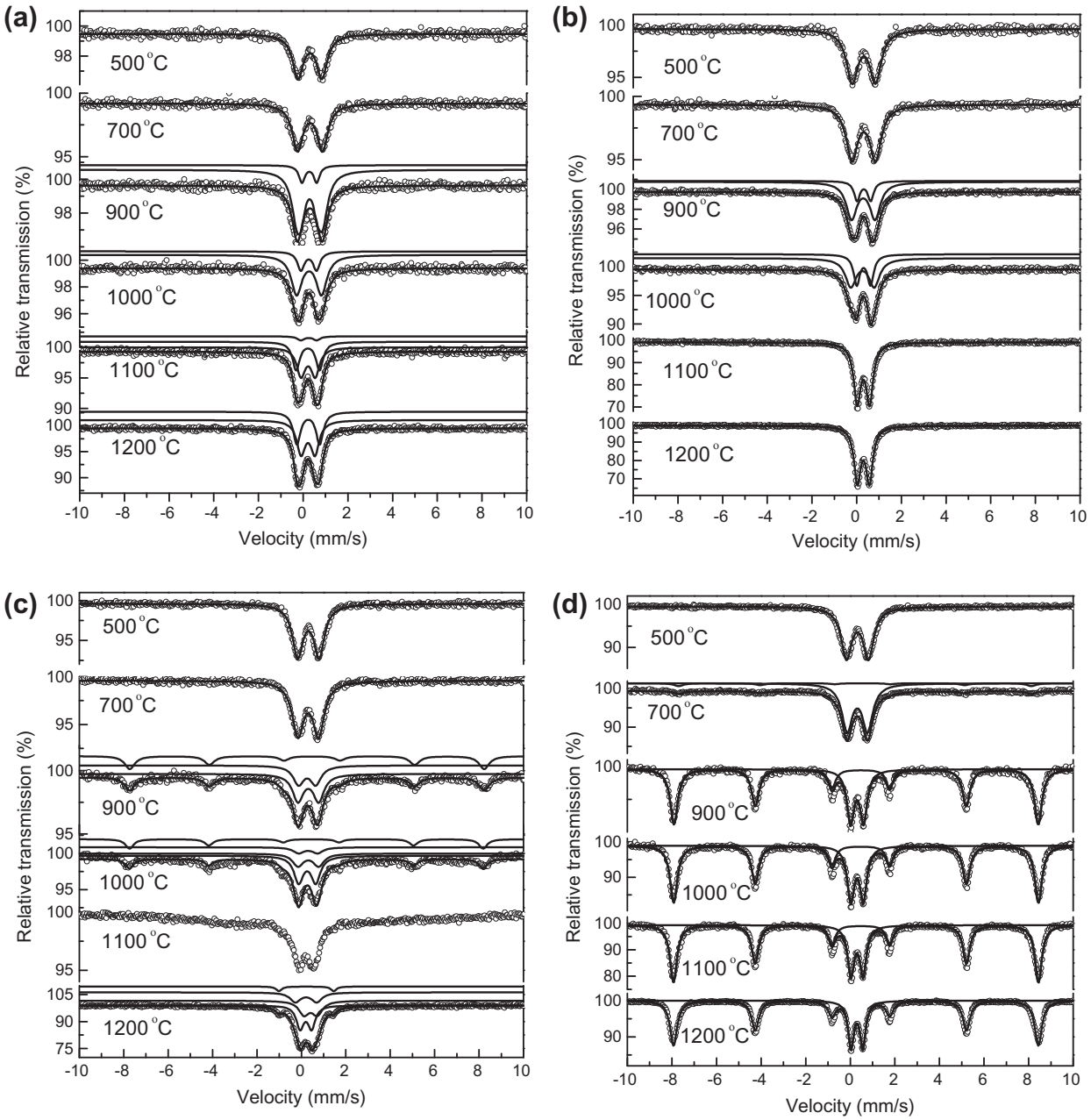

Fig. 5. Room temperature ^{57}Fe Mössbauer spectra of: (a) BF1A-*t*, (b) F1A-*t*, (c) BF3A-*t*, and (d) F3A-*t* samples.

cated that a high Fe^{3+} concentration in BF3A made the small superparamagnetic Fe_2O_3 easier to aggregate and form into relatively large Fe_2O_3 particles with the elevation of calcination temperature. With regard to Fe^{3+}(Th) in $BaAl_2O_4$, the QS value in BF3A-900 was higher than that in BF1A-900 (0.77 vs. 0.66 mm/s, Table 3), indicating the larger structural deformation due to more Fe^{3+} ions incorporated into the $BaAl_2O_4$ structure. In addition, the value of the hyperfine field (H = 494.8 kOe) corresponding to Fe_2O_3 in BF3A-900 was much smaller than that of bulk Fe_2O_3 (518 ± 6 kOe) [38], indicating that an appropriate number of nonmagnetic Ba^{2+} and/or Al^{3+} ions entered into the Fe_2O_3 lattice. It should be stressed that further calcination at 1000 °C resulted in a decrease of relative areas (A) for both the sextuplet and the doublet corresponding to Fe_2O_3 from 35 and 39% to 27 and 22%, respectively, accompanied by the appearance of a doublet assigned to Fe^{3+} in the newly formed hexaaluminate phase. Especially, when the calcination temperature increased to 1100 and 1200 °C, with hexaaluminate becoming the major phase, one can obviously see that the sextuplet intensity significantly decreased and eventually disappeared. Considering that there was no Fe loss during the calcination, as indicated by XRF analysis, Fe^{3+} ions originated from Fe_2O_3 particles should enter into the hexaaluminate structure. The spectrum of BF3A-1200 was fitted with four quadruple splitting doublets (Fig. 5c, Table 3). Like that of BF1A-1200, besides a doublet (24%) corresponding to Fe^{3+}(Th) in the distorted Al(5) site of the β_I-Al_2O_3 phase, one doublet (38%) with IS = 0.20 mm/s and QS = 0.56 mm/s was assigned to tetrahedral Fe^{3+} ions in symmetric Al(2) sites in the spinel blocks of both β_I-Al_2O_3 and MP phases, associated with the identical occupation of Al(2) sites by Fe^{3+} ions in both phases of BF3A-1200, as revealed by the Rietveld refinement results (Table 2). Furthermore, two new doublets with entirely different Mössbauer parameters were also observed, due to

Table 3
Room temperature ^{57}Fe Mössbauer parameters of BF1A-*t*, F1A-*t*, BF3A-*t*, and F3A-*t*.

Samples	IS[a] (mm/s)	QS[b] (mm/s)	H[c] (KOe)	A[d] (%)	Assignment
BF1A-500	0.30	1.07	–	100	Fe^{3+} (low concentration)
BF1A-700	0.31	1.11	–	100	Fe^{3+} (low concentration)
BF1A-900	0.30	1.11	–	83	Fe^{3+} (low concentration)
	0.27	0.66	–	17	Fe^{3+}(Th) in $BaAl_2O_4$
BF1A-1000	0.26	1.11	–	75	Fe^{3+} (low concentration)
	0.25	0.70	–	25	Fe^{3+}(Th) in $BaAl_2O_4$
BF1A-1100	0.21	1.03	–	49	Fe^{3+}(Th) in Al(5) of β_l-Al_2O_3
	0.20	0.60	–	45	Fe^{3+}(Th) in Al(2) of β_l-Al_2O_3
	0.25	0.71	–	6	Fe^{3+}(Th) in $BaAl_2O_4$
BF1A-1200	0.23	1.01	–	49	Fe^{3+}(Th) in Al(5) of β_l-Al_2O_3
	0.21	0.60	–	51	Fe^{3+}(Th) in Al(2) of β_l-Al_2O_3
F1A-500	0.32	1.04	–	100	Fe^{3+} (low concentration)
F1A-700	0.32	1.05	–	100	Fe^{3+} (low concentration)
F1A-900	0.30	1.05	–	77	Fe^{3+} (low concentration)
	0.32	0.61	–	23	Fe^{3+} in θ-Al_2O_3
F1A-1000	0.26	1.05	–	62	Fe^{3+} (low concentration)
	0.31	0.62	–	38	Fe^{3+} in θ-Al_2O_3
F1A-1100	0.30	0.55	–	100	Fe^{3+} in α-Al_2O_3
F1A-1200	0.30	0.54	–	100	Fe^{3+} in α-Al_2O_3
BF3A-500	0.32	0.96	–	100	Fe^{3+} (high concentration)
BF3A-700	0.31	0.93	–	100	Fe^{3+} (high concentration)
BF3A-900	0.36	−0.23	494.8	35	Fe^{3+} (high concentration)
	0.31	0.93	–	39	
	0.26	0.77	–	26	Fe^{3+}(Th) in $BaAl_2O_4$
BF3A-1000	0.33	−0.22	493.8	27	Fe^{3+} (high concentration)
	0.31	0.93	–	22	
	0.26	0.77	–	41	Fe^{3+}(Th) in $BaAl_2O_4$
	0.30	0.85	–	10	Fe^{3+} in Hexa[e]
BF3A-1200	0.21	0.93	–	24	Fe^{3+}(Th) in Al(5) of β_l-Al_2O_3
	0.20	0.56	–	38	Fe^{3+}(Th) in Al(2) of both β_l-Al_2O_3 and MP
	0.41	0.60	–	31	Fe^{3+}(Oh) in MP
	0.22	2.47	–	7	Fe^{3+}(Tr) in MP
F3A-500	0.32	0.98	–	100	Fe^{3+} (high concentration)
F3A-700	0.32	0.92	–	90	Fe^{3+} (high concentration)
	0.38	−0.33	490.4	10	
F3A-900	0.37	−0.21	506.6	70	Fe^{3+} (high concentration)
	0.30	0.58	–	30	Fe^{3+} in α-Al_2O_3
F3A-1000	0.37	−0.21	507.2	70	Fe^{3+} (high concentration)
	0.30	0.56	–	30	Fe^{3+} in α-Al_2O_3
F3A-1100	0.36	−0.22	507.5	72	Fe^{3+} (high concentration)
	0.30	0.54	–	28	Fe^{3+} in α-Al_2O_3
F3A-1200	0.36	−0.22	507.3	71	Fe^{3+} (high concentration)
	0.30	0.53	–	29	Fe^{3+} in α-Al_2O_3

[a] Isomer shift relative to α-Fe.
[b] Quadrupole splitting.
[c] Hyperfine field.
[d] Relative area.
[e] Both β_l-Al_2O_3 and MP hexaaluminates; uncertainty is ±5% of reported value.

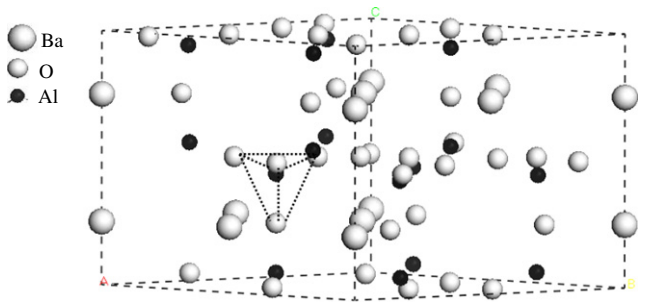

Fig. 6. The crystal structure of $BaAl_2O_4$.

the formation of MP structure. The IS value (0.41 mm/s) of one doublet (31%) was close to the reported value (0.42 mm/s) corresponding to Fe^{3+} ions in octahedral (Oh) sites of MP-type hexaaluminate [34], which was higher than that of Fe^{3+}(Th) due to the larger band separation of Fe^{3+} and O^{2-} for Oh sites. Considering the Rietveld refinement results (Table 2), the Fe^{3+}(Oh) doublet was assigned to Fe^{3+} ions in the octahedral Al(1), Al(3), and Al(4) sites in the MP structure (Fig. 4b). The other doublet (7%), with a very high QS value (2.47 mm/s), was assigned to Fe^{3+} ions in the much distorted trigonal bipyramidal Al(5) sites (denoted as Tr) in the mirror plane of the MP structure (Fig. 4b). In fact, QS of this order has also been observed at the Tr site in BF2A-1200 containing 18% MP phase (not shown here), MP-type $CaFe_xAl_{12-x}O_{19}$ [34], and $BaFe_{12}O_{19}$ [42]. According to the hyperfine parameters and the BF1A-*t* results (Table 3), tetrahedral Fe^{3+} ions originated from the spinel-type $BaAl_2O_4$ phase in the BF3A-*t* precursor (1000 °C calcination) entered into the tetrahedral Al(2) sites in the spinel blocks of both β_l-Al_2O_3 and MP phases. This was further supported by the close relative area (A) of Fe^{3+}(Th) in $BaAl_2O_4$ (41%) of BF3A-1000 and Fe^{3+}(Th) in Al(2) sites in both hexaaluminate structures (38%) of BF3A-1200. With regard to Fe^{3+} ions in oxidic entities dispersed on the Ba-modified γ-Al_2O_3, Fe^{3+} ions in smaller portions entered into the distorted Al(5) sites in the β_l-Al_2O_3 phase, since such sites originating from the Reidinger defect were very limited. Meanwhile, Fe^{3+} ions in larger portions entered into the Oh (Al(1), Al(3), and Al(4)) and Tr (Al(5)) sites in the newly formed MP struc-

ture. As only the Al(3) and Al(5) sites were largely occupied by Fe^{3+} ions, with site occupancies above 60% (Table 2), Fe^{3+} ions in larger portions should preferentially enter into the Al(3) and Al(5) sites, both of which are in the mirror plane of the MP structure.

In the case of F3A-*t* (Fig. 5d), only the doublet assigned to small superparamagnetic Fe_2O_3 species was observed in F3A-500. After 700 °C calcination, a combination of 90% superparamagnetic doublet and 10% magnetic sextet appeared, indicating the increased particle size of Fe_2O_3. When the calcination temperature increased above 900 °C, the doublet (≈30%) assigned to Fe^{3+} ions in α-Al_2O_3 was observed as that of F1A-1100 and F1A-1200. The relative area of the sextet corresponding to Fe_2O_3, with crystalline size 25–46 nm, was rather high (⩾70%), indicating that most of the Fe^{3+} species had severely sintered. Comparing this fact with the evolution of Mössbauer spectra from sextuplet to doublet observed in BF3A-*t*, we can infer that the formation of hexaaluminate is of crucial importance for the high dispersion of active Fe^{3+} species under high-temperature conditions.

In the hexaaluminate structure, framework Fe is always coordinated with lattice oxygen, the mobility of which plays an important role in oxygen-involving reactions [5,43–45]. Fig. 7 displays ^{57}Fe Mössbauer spectra of BF1A-1200 and BF3A-1200 samples after H_2 reduction at 350 °C, and the corresponding Mössbauer parameters are listed in Table 4. It should be pointed out that, in the reduced samples, one iron component with IS = 0.91–0.98 mm/s was assigned to Fe^{2+} species [38,39]. In comparison with the relative area (*A*) of Fe^{3+} ions in the Al(2) and Al(5) sites of β$_l$-Al_2O_3 over BF1A-1200 (51% and 49%, Table 3), the corresponding values decreased to 41% and 28% after H_2 reduction. Obviously, Fe^{3+} ions in the Al(5) sites in the mirror plane were much more easily reduced than those in the Al(2) sites in the spinel block, indicating the greater mobility of lattice oxygen coordinated with Fe^{3+} in Al(5) site in the mirror plane of the β$_l$-Al_2O_3 structure. This was in agreement with the observation that the mirror plane was a preferential diffusion route of oxygen, based on the measurement of anisotropic diffusion of ^{18}O [46,47]. As for BF3A-1200, besides Fe^{3+}(Th) in Al(5) in the mirror plane of β$_l$-Al_2O_3, Fe^{3+}(Oh) in the MP phase was also found to be easily reduced and the corresponding *A* value decreased significantly from 31% to 20%. Among the three kinds of Oh sites (Al(1), Al(3), and Al(4)) in the MP structure (Fig. 4b), Fe^{3+}(Oh) ions in Al(3) sites in the mirror plane should be preferentially reduced, considering the greater mobility and easier diffusion of oxygen in the mirror plane. Fe^{3+} ions in Al(5) sites in β$_l$-Al_2O_3 and Al(3) sites in the MP phase, both of which are inlaid in the mirror plane, should be more interesting for catalytic activity toward oxygen-involving reaction.

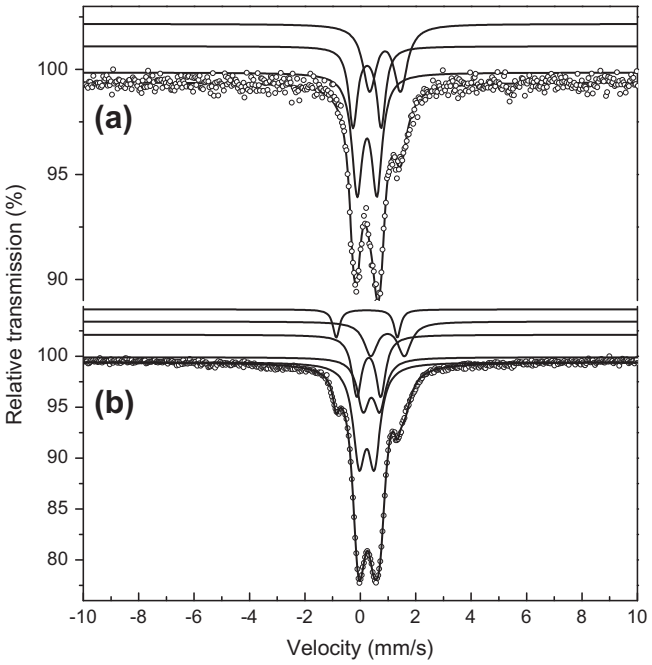

Fig. 7. Room temperature ^{57}Fe Mössbauer spectra of: (a) BF1A-1200 after H_2 reduction at 350 °C for 2 h and (b) BF3A-1200 after H_2 reduction at 350 °C for 4 h.

3.4. Morphology

Table 5 lists the BET surface areas of BF1A-*t*, F1A-*t*, BF3A-*t*, and F3A-*t*. As expected, the BET surface areas of these samples decreased continuously with the elevation of the calcination temperature. In particular, significant sintering occurred, accompanied by phase transformations. For example, significant loss of surface area took place when BF1A and F1A samples were calcined at 1100 °C. As described above, phase transformation started at this temperature: γ-Al_2O_3 and $BaAl_2O_4$ were transformed into hexaaluminate for the BF1A sample, while metastable θ-Al_2O_3 was transformed into thermally stable α-Al_2O_3 for F1A. In addition, the increase of Fe content resulted in the loss of specific surface areas at the same

Table 5
BET surface areas of BF1A-*t*, F1A-*t*, BF3A-*t*, and F3A-*t* samples.

Calcination temperature (°C)	Surface area (m^2/g)			
	BF1A	F1A	BF3A	F3A
500	301	345	230	276
700	188	235	167	201
900	108	132	81	32
1000	88	92	47	15
1100	30	12	21	6
1200	18	7	17	6

Table 4
Room temperature ^{57}Fe Mössbauer parameters of BF1A-1200 after H_2 reduction at 350 °C for 2 h and BF3A-1200 after H_2 reduction at 350 °C for 4 h.

Samples	IS[a] (mm/s)	QS[b] (mm/s)	A[c] (%)	Assignment
BF1A-1200	0.25	0.98	28	Fe^{3+}(Th) in Al(5) of β$_l$-Al_2O_3
	0.23	0.62	41	Fe^{3+}(Th) in Al(2) of β$_l$-Al_2O_3
	0.91	1.11	31	Fe^{2+}
BF3A-1200	0.30	0.86	20	Fe^{3+}(Th) in Al(5) of β$_l$-Al_2O_3
	0.23	0.55	38	Fe^{3+}(Th) in Al(2) of both β$_l$-Al_2O_3 and MP
	0.41	0.60	20	Fe^{3+}(Oh) in MP
	0.23	2.20	7	Fe^{3+}(Tr) in MP
	0.98	1.23	15	Fe^{2+}

[a] Isomer shift relative to α-Fe.
[b] Quadrupole splitting.
[c] Relative area; uncertainty is ±5% of reported value.

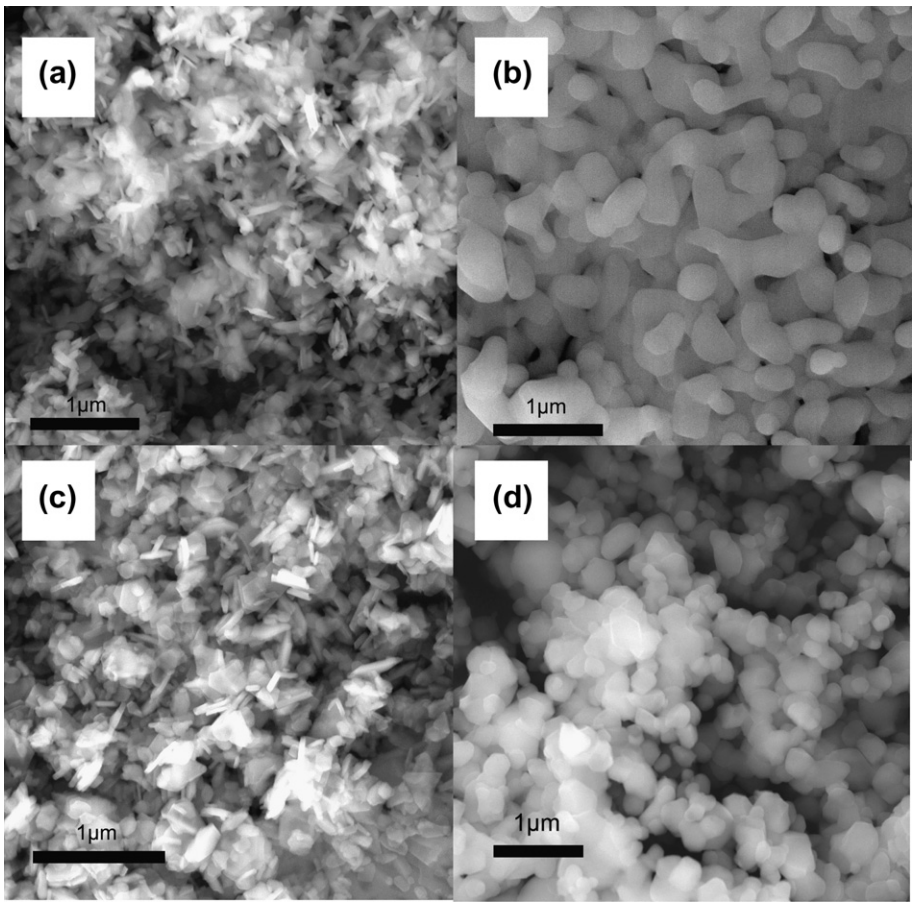

Fig. 8. Scanning electron micrographs of: (a) BF1A-1200, (b) F1A-1200, (c) BF3A-1200, and (d) F3A-1200 samples.

calcination temperature, due to the overlay of Fe_2O_3 particles and the promoting effect of Fe on phase transformation. However, after 1200 °C calcination with the formation of a pure hexaaluminate phase, the surface areas of BF*x*A-1200 (*x* = 0–4) did not show any significant variation with increasing *x* value, but slightly decreased from 20 m^2/g at *x* = 0 to 17 m^2/g at *x* = 2 and 16 m^2/g at *x* = 4. It must be stressed that the surface areas of BF1A-1200 and BF3A-1200 were almost three times larger than those of F1A-1200 and F3A-1200, demonstrating the outstanding sintering resistance of hexaaluminates. This could be further visualized from the SEM images in Fig. 8. In contrast with the extensive sintering of F1A-1200 and F3A-1200, BF1A-1200 and BF3A-1200 showed small anisotropic planar crystallites and the planar facet had orientations parallel to the mirror plane due to the peculiar layered structure of hexaaluminate.

3.5. Catalytic activity

Fig. 9 depicts the profiles of 30 vol.% N_2O conversion vs. reaction temperature over BF*x*A-1200 (*x* = 0–4), F1A-1200, and F3A-1200 samples. In the absence of Fe (*x* = 0), the BA-1200 did not exhibit activity toward N_2O decomposition until 700 °C. A slight enhancement of the catalytic activity was observed on F1A-1200 and F3A-1200 with the N_2O conversion of 22% at 700 °C. When Fe was incorporated into the hexaaluminate structure (*x* = 1 and 2), the activity was enhanced significantly and N_2O conversion at 700 °C could attain 74% and 97%, respectively, suggesting that the framework Fe species were highly active for N_2O decomposition. As Fe content increased from *x* = 2 to 4, the activity increased further,

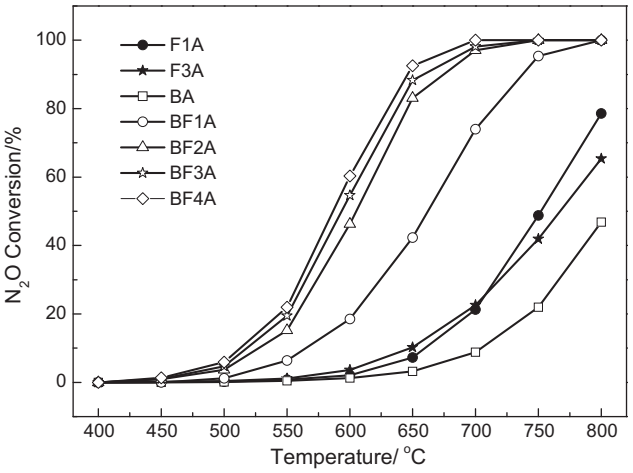

Fig. 9. N_2O conversion as a function of reaction temperature over BF*x*A-1200 (*x* = 0–4), F1A-1200, and F3A-1200 catalysts.

but the positive effect of framework Fe species became less remarkable.

4. Discussion

In the β_l-Al_2O_3 structure of BF*x*A-1200 (*x* = 1–4), Fe^{3+} ions occupied the tetrahedral Al(2) sites with good symmetry in the spinel block, and in the mirror plane only the distorted tetrahedral interstitial Al(5) sites could be occupied, while substitution was rare in

the symmetric tetrahedral Al(3) sites. In the MP structure, the well symmetric Al(2) site was also largely occupied by Fe^{3+} in the spinel block. In the mirror plane, besides the distorted trigonal bipyramidal Al(5) sites, the octahedral Al(3) sites, which can offer a larger space to accommodate larger Fe^{3+} ions, as compared with the smaller tetrahedral Al(3) in β_l-Al_2O_3, were also preferentially occupied. In a word, for both β_l-Al_2O_3 and MP structures, Fe^{3+} ions in the spinel block tended to occupy symmetric tetrahedral Al(2) sites with small space, while in the mirror plane the distorted sites (Al(5) in both β_l-Al_2O_3 and MP) and the sites with large space (octahedral Al(3) in MP) easily underwent substitution. Such a difference should originate from different Fe species in the precursors, that is, Fe^{3+}(Th) in $BaAl_2O_4$ and Fe^{3+} ions in oxidic entities dispersed on Ba-modified γ-Al_2O_3.

Groppi et al. [25] proposed two routes for the formation of Ba hexaaluminate prepared by the coprecipitation method herein adopted: solid-state reactions between γ-Al_2O_3 and $BaAl_2O_4$, or dispersed barium compounds. Based on the strong structural similarity of spinel-type $BaAl_2O_4$ to the spinel block of hexaaluminate, the tetrahedral Fe^{3+} ions in the intermediate $BaAl_2O_4$ phase should have priority to enter into the tetrahedral Al(2) sites in the spinel block of hexaaluminate, rather than migrating into larger octahedral Al(1) and Al(4) sites. The observed preferential occupancy of Fe^{3+} in the Al(2) site instead of the Al(1) and Al(4) sites in the spinel block supported this statement. On the other hand, Fe^{3+} ions originated from oxidic entities dispersed on Ba-modified γ-Al_2O_3 should prefer to enter into the Ba-containing mirror plane via the diffusion of barium ions in γ-Al_2O_3, since the mirror plane is loosely packed in a way favorable to ion diffusion [46,47]. The observed preferential occupancy of distorted Al(5) (both β_l-Al_2O_3 and MP) and large octahedral Al(3) (MP) instead of symmetric tetrahedral Al(3) with small space (β_l-Al_2O_3) supported this viewpoint. In particular, Fe^{3+} ions at low concentration preferentially occupied the distorted interstitial Al(5) sites in the mirror plane of the β_l-Al_2O_3 phase; meanwhile, Fe^{3+} ions at high concentration mainly entered into the Al(3) and Al(5) sites in the mirror plane of MP phase.

Fig. 10 shows the schematic diagram of Fe evolution from precursors to different crystallographic sites of Fe-substituted Ba hexaaluminates. Initially, Fe species were highly dispersed on Ba-modified γ-Al_2O_3 existing as oxidic entities. With the formation of an intermediate $BaAl_2O_4$ phase with increasing calcination temperature, Fe^{3+} ions originated from oxidic entities partially migrated into the tetrahedral Al sites in the $BaAl_2O_4$ structure. When β_l-Al_2O_3- and/or MP-type hexaaluminates formed at higher calcination temperature, depending on Fe^{3+} concentration, Fe^{3+} ions originated from oxidic entities mainly entered into the sites in the loosely packed mirror plane of hexaaluminates via the diffusion of Ba^{2+} in γ-Al_2O_3. In particular, Fe^{3+} ions at low concentration preferentially entered into the distorted tetrahedral Al(5) sites of the β_l-Al_2O_3 phase, while Fe^{3+} ions at high concentration mainly entered into the distorted trigonal bipyramidal Al(5) and octahedral Al(3) sites with large space in MP phase. Meanwhile, Fe^{3+} ions in the tetrahedral sites of spinel-type $BaAl_2O_4$ preferentially entered into the tetrahedral Al(2) sites in the spinel block of hexaaluminates.

An attempt has been made to correlate the intrinsic activities (mol N_2O converted per hour and per square meter) of BF*x*A-1200 (*x* = 1–4) catalysts at 550 °C with the number of Fe^{3+} ions in different crystallographic sites of both β_l-Al_2O_3 and MP phases identified in the present study (Fig. 11). When *x* = 1, all Fe^{3+} ions were located in the β_l-Al_2O_3 phase and the intrinsic activity was significantly enhanced compared with the Fe-free BA-1200 sample, implying that Fe^{3+} ions in the β_l-Al_2O_3 structure were responsible for N_2O decomposition. When *x* = 2, most of the Fe^{3+} ions were still located in the β_l-Al_2O_3 phase and a small fraction of the Fe^{3+} ions started to enter into the newly formed MP phase. Meanwhile, the intrinsic activity increased significantly further. Increasing *x* to 3 and 4 resulted in a decrease of the Fe^{3+} amount in β_l-Al_2O_3, while the Fe^{3+} amount in the MP phase continued to increase, accompanied by enhanced intrinsic activity. In particular, when *x* = 4 with most of the Fe^{3+} ions in the MP phase, the highest intrinsic activity

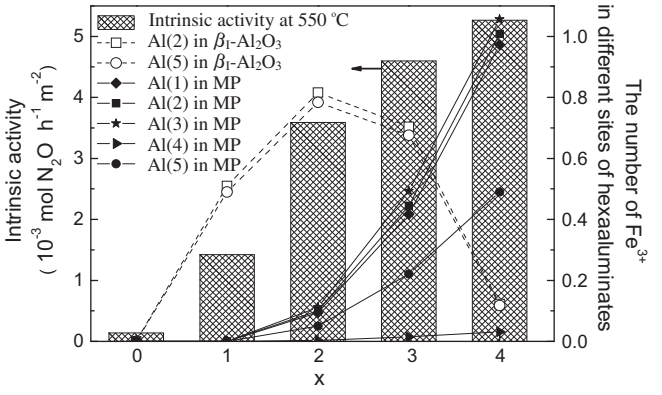

Fig. 11. The intrinsic activity at 550 °C and the number of Fe^{3+} at different crystallographic sites of both β_l-Al_2O_3 and MP hexaaluminates as a function of *x* values in BF*x*A-1200 (*x* = 0–4) catalysts.

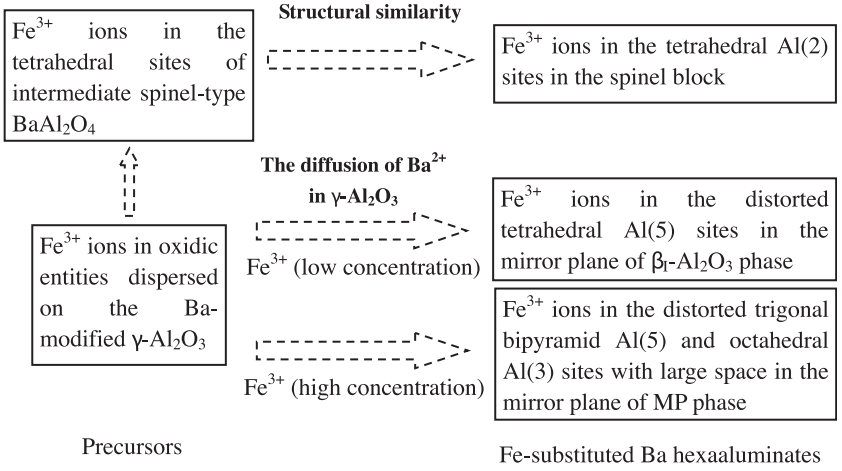

Fig. 10. The schematic diagram of Fe evolution from precursors to different crystallographic sites of Fe-substituted BF*x*A (*x* = 1–4) hexaaluminates.

was observed. These results strongly suggested that the transformation of Fe^{3+} ions from β_l-Al_2O_3 to the MP phase further improved the intrinsic activity.

According to the literature [48–52], the decomposition of N_2O can be described as the adsorption of N_2O at the active centers, usually coordinatively unsaturated surface transition metal ions, with the formation of N_2 and a surface O. Subsequently, this surface oxygen desorbs either by combination with another surface oxygen or by direct reaction with another N_2O. Based on this mechanism, there are two main factors affecting the N_2O decomposition activity of Fe-substituted hexaaluminates: the adsorption of N_2O onto surface Fe ions and the desorption of oxygen. Considering that the loosely packed mirror plane is a preferential exposure surface [29,32], Fe ions incorporated into the sites in the mirror plane (Al(5) in both β_l-Al_2O_3 and MP, Al(3) in MP) were more easily accessible to the gas-phase N_2O molecules and favorable for the adsorption of N_2O, compared with those in the deep positions (Al(2) in both β_l-Al_2O_3 and MP, Al(1) and Al(4) in MP) in the rigid spinel block. Moreover, our H_2-reduced Mössbauer results showed that the oxygen coordinated with Fe ions in specific sites (Al(5) in β_l-Al_2O_3 and Al(3) in MP) in the mirror plane much more easily moved and diffused, thus greatly facilitating the desorption of surface oxygen generated by the dissociative adsorption of N_2O onto the adjacent coordinated Fe ions, since oxygen desorption is generally accepted as the rate-determining step for N_2O decomposition process [44,48,53,54]. Therefore, Fe ions in Al(5) sites of β_l-Al_2O_3 and Al(3) sites of MP phase, both of which are inlaid in the preferentially exposed mirror plane and coordinated with active oxygen, should be highly active for N_2O decomposition. For the BF*x*A-1200 (x = 1–4) catalysts, when x = 1 and 2, the observed significantly increased intrinsic activity could be attributed to Fe ions in Al(5) sites in the β_l-Al_2O_3 phase, while Fe ions in Al(3) sites in the MP phase were mainly responsible for the continuous enhancement of intrinsic activity with increasing x up to 3 and 4.

5. Conclusion

In summary, we have given a clear picture of the mechanism of stabilization of Fe^{3+} ions in β_l-Al_2O_3 and MP-type Fe-substituted barium hexaaluminates. Fe^{3+} ions originated from oxidic entities dispersed on Ba-modified γ-Al_2O_3 mainly entered into the sites in the loosely packed mirror plane of the hexaaluminates. In particular, Fe^{3+} ions at low concentration preferentially entered into the distorted tetrahedral Al(5) sites of β_l-Al_2O_3 phase, while Fe^{3+} ions at high concentration mainly entered into the distorted trigonal bipyramidal Al(5) and octahedral Al(3) sites with large spaces in the MP phase. Meanwhile, tetrahedral Fe^{3+} ions in intermediate spinel-type $BaAl_2O_4$ preferentially entered into the tetrahedral Al(2) sites in the spinel block of hexaaluminates. Fe ions in the Al(5) sites of β_l-Al_2O_3 and the Al(3) sites of MP phase should be highly active for N_2O decomposition.

Acknowledgments

Financial support from National Science Foundation of China (NSFC) Grants (20773122, 20773124, and 21076211), the External Cooperation Program of Chinese Academy of Sciences (GJHZ200827), and the Chinese Academy of Sciences for the "100 Talents" project is gratefully acknowledged.

References

[1] H. Arai, M. Machida, Appl. Catal. A 138 (1996) 161.
[2] K. Eguchi, H. Arai, Catal. Today 29 (1996) 379.
[3] X.G. Ren, J.D. Zheng, Y.J. Song, P. Liu, Catal. Commun. 9 (2008) 807.
[4] P. Artizzu-Duart, Y. Brullé, F. Gaillard, E. Garbowski, N. Guilhaume, M. Primet, Catal. Today 54 (1999) 181.
[5] S.Q. Li, H.T. Liu, L. Yan, X.L. Wang, Catal. Commun. 8 (2007) 237.
[6] Z.L. Xu, M. Zhen, Y.L. Bi, K.J. Zhen, Catal. Lett. 64 (2000) 157.
[7] W.L. Chu, W.S. Yang, L.W. Lin, Appl. Catal. A 235 (2002) 39.
[8] R. Kikuchi, Y. Iwasa, T. Takeguchi, K. Eguchi, Appl. Catal. A 281 (2005) 61.
[9] T.H. Gardner, J.J. Spivey, A. Campos, J.C. Hissam, E.L. Kugler, A.D. Roy, Catal. Today 157 (2010) 166.
[10] M. Santiago, M.A.G. Hevia, J. Pérez-Ramírez, Appl. Catal. B 90 (2009) 83.
[11] J. Pérez-Ramírez, M. Santiago, Chem. Commun. (2007) 619.
[12] M. Santiago, J. Pérez-Ramírez, Environ. Sci. Technol. 41 (2007) 1704.
[13] S.M. Zhu, X.D. Wang, A.Q. Wang, Y. Cong, T. Zhang, Chem. Commun. (2007) 1695.
[14] S.M. Zhu, X.D. Wang, A.Q. Wang, T. Zhang, Catal. Today 131 (2008) 339.
[15] M. Tian, A.Q. Wang, X.D. Wang, Y.Y. Zhu, T. Zhang, Appl. Catal. B 92 (2009) 437.
[16] M. Tian, X.D. Wang, Y.Y. Zhu, J.H. Wang, T. Zhang, Chin. J. Catal. 31 (2010) 100.
[17] M. Machida, K. Eguchi, H. Arai, J. Catal. 120 (1989) 377.
[18] L. Lietti, C. Cristiani, G. Groppi, P. Forzatti, Catal. Today 59 (2000) 191.
[19] G. Groppi, C. Cristiani, P. Forzatti, Appl. Catal. B 35 (2001) 137.
[20] P. Artizzu-Duart, J.M. Millet, N. Guilhaume, E. Garbowski, M. Primet, Catal. Today 59 (2000) 163.
[21] S.Q. Li, X.L. Wang, J. Alloys Compd. 432 (2007) 333.
[22] M. Astier, E. Garbowski, M. Primet, Catal. Lett. 95 (2004) 31.
[23] G. Groppi, C. Cristiani, P. Forzatti, J. Catal. 168 (1997) 95.
[24] D. Naoufal, J.-M. Millet, E. Garbowski, Y. Brullé, M. Primet, Catal. Lett. 54 (1998) 141.
[25] G. Groppi, C. Cristiani, P. Forzatti, M. Bellotto, J. Mater. Sci. 29 (1994) 3441.
[26] G. Groppi, M. Bellotto, C. Cristiani, P. Forzatti, J. Mater. Sci. 34 (1999) 2609.
[27] M.S. Yalfani, M. Santiago, J. Pérez-Ramírez, J. Mater. Chem. 17 (2007) 1222.
[28] G. Groppi, M. Bellotto, C. Cristiani, P. Forzatti, P.L. Villa, Appl. Catal. A 104 (1993) 101.
[29] M. Bellotto, G. Artioli, C. Cristiani, P. Forzatti, G. Groppi, J. Catal. 179 (1998) 597.
[30] P. Artizzu, N. Guilhaume, E. Garbowski, Y. Brullé, M. Primet, Catal. Lett. 51 (1998) 69.
[31] N. Iyi, Z. Inoue, S. Takekawa, S. Kimura, J. Solid State Chem. 52 (1984) 66.
[32] G. Groppi, F. Assandri, M. Bellotto, C. Cristiani, P. Forzatti, J. Solid State Chem. 114 (1995) 326.
[33] N. Iyi, S. Takekawa, S. Kimura, J. Solid State Chem. 83 (1989) 8.
[34] F.P. Glasser, F.W.D. Woodhams, R.E. Meads, W.G. Parker, J. Solid State Chem. 5 (1972) 255.
[35] H. El Shinawi, J.F. Marco, F.J. Berry, C. Greaves, J. Mater. Chem. 20 (2010) 3253.
[36] F.J. Berry, D. Eadon, J. Holloway, L.E. Smart, J. Mater. Chem. 6 (1996) 221.
[37] K. Liu, A.Q. Wang, W.S. Zhang, J.H. Wang, Y.Q. Huang, J.Y. Shen, T. Zhang, J. Phys. Chem. C 114 (2010) 8533.
[38] X.D. Wang, X.Q. Zhao, J.Y. Shen, X.Y. Sun, T. Zhang, L.W. Lin, Phys. Chem. Chem. Phys. 4 (2002) 2846.
[39] R.G. Burns, Hyperfine Interact. 91 (1994) 739.
[40] J. Martynczuk, F.Y. Liang, M. Arnold, V. Šepelák, A. Feldhoff, Chem. Mater. 21 (2009) 1586.
[41] E. Tronc, F. Laville, M. Gasperin, A.M. Lejus, D. Vivien, J. Solid State Chem. 81 (1989) 192.
[42] A.G. Belous, O.I. V'yunov, E.V. Pashkova, V.P. Ivanitskii, O.N. Gavrilenko, J. Phys. Chem. B 110 (2006) 26477.
[43] Y.Q. Huang, A.Q. Wang, L. Li, X.D. Wang, D.S. Su, T. Zhang, J. Catal. 255 (2008) 144.
[44] D.V. Ivanov, E.M. Sadovskaya, L.G. Pinaeva, L.A. Isupova, J. Catal. 267 (2009) 5.
[45] V.N. Stathopoulos, V.C. Belessi, T.V. Bakas, S.G. Neophytides, C.N. Costa, P.J. Pomonis, A.M. Efstathiou, Appl. Catal. B 93 (2009) 1.
[46] M. Machida, A. Sato, T. Kijima, H. Inoue, K. Eguchi, H. Arai, Catal. Today 26 (1995) 239.
[47] M. Machida, T. Shiomitsu, K. Eguchi, H. Arai, Y. Shimizu, J. Solid State Chem. 95 (1991) 220.
[48] F. Kapteijn, J. Rodriguez-Mirasol, J.A. Moulijn, Appl. Catal. B 9 (1996) 25.
[49] F. Kapteijn, G. Marbán, J. Rodriguez-Mirasol, J.A. Moulijn, J. Catal. 167 (1997) 256.
[50] C.M. Fu, V.N. Korchar, W.K. Hall, J. Catal. 68 (1981) 166.
[51] J.A. Ryder, A.K. Chakraborty, A.T. Bell, J. Phys. Chem. B 106 (2002) 7059.
[52] J.A. Ryder, A.K. Chakraborty, A.T. Bell, J. Catal. 220 (2003) 84.
[53] B.R. Wood, J.A. Reimer, A.T. Bell, M.T. Janicke, K.C. Ott, J. Catal. 224 (2004) 148.
[54] H.K. Cheng, Y.Q. Huang, A.Q. Wang, L. Li, X.D. Wang, T. Zhang, Appl. Catal. B 89 (2009) 391.